Journal of Computational Physics 228 (2009) 7729–7741

Contents lists available at ScienceDirect

Journal of Computational Physics

journal homepage: www.elsevier.com/locate/jcp

A new phase-screen method for electromagnetic wave propagation in turbulent flows using large-eddy simulation

A. Dipankar *, P. Sagaut

Institut Jean le Rond d'Alembert – UMR CNRS 7190, Université Pierre et Marie Curie – Paris 6, 4 place Jussieu – Case 162, F-75252 Paris, cedex 5, France

ARTICLE INFO

Article history:
Received 30 January 2009
Received in revised form 30 April 2009
Accepted 13 July 2009
Available online 24 July 2009

Keywords:
Large-eddy simulation
Atmospheric turbulence
Radio wave propagation
Phase-screen method

ABSTRACT

Use of large-eddy simulation (LES) data in electromagnetic wave propagation modeling is not very common because of the high computational cost involved. A new phase-screen method is proposed to model radio wave propagation, in the atmospheric turbulence, using the resolved scale refractivity obtained from LES. The proposed method offers the same level of accuracy, as the one already existing in the literature, at much cheaper cost.

1. Introduction

The numerical modeling of electromagnetic (EM) wave propagation is performed either using the mean field information, as obtained from the field experiments [1–3], or using a complete statistical approach [4–7], known as multiple phase-screen method. In multiple phase-screen method, the extended random media is represented in terms of equally spaced thin phase-screens. Phase is artificially generated by filtering Gaussian distribution white noise according to the desired phase spectrum, which in turn is related to the refractive index spectrum. Phase-screens thus generated are uncorrelated in the propagation direction and hence the method is also known as independent phase-screen method. Because of its complete statistical nature, we will refer to this method as statistical phase-screen method (SPSM).

The only limitation of SPSM is that it requires correct description of the refractive index spectrum at all scales. It is widely known that there is no universality in the behavior of the refractive index spectrum, either in lower wave number region (scales larger than L_0) or in the higher wave number (scales smaller than l_0). Here L_0 is the outer scale and l_0 is the inner scale of the turbulent scalar field. A schematic view of the refractive index spectrum, showing relevant length scales of turbulence, is displayed in Fig. 1 for reference. The analytical form of spectrum, for these large scales, is at best a rough approximation and for smaller scales, a good approximation. The physical meaning various length scales, relevant for the present work, is provided in Table 1 for reference. Reader is suggested to refer to this table to have better understanding of the discussions in the following sections.

From the discussions above it is clear that we need to be particularly careful with the behavior of the scales larger than L_0. Behavior of these large scales vary depending on the flow conditions, and it can be best described with the help of instantaneous field distribution and not with the statistical approach discussed above. Instantaneous field data can only be obtained either experimentally or numerically. There are some field experiments performed in the past [8,9] in which the

* Corresponding author.
E-mail addresses: dipankar@lmm.jussieu.fr, dipankar.anurag@gmail.com (A. Dipankar), pierre.sagaut@upmc.fr (P. Sagaut).

0021-9991/$ - see front matter © 2009 Elsevier Inc. All rights reserved.
doi:10.1016/j.jcp.2009.07.011

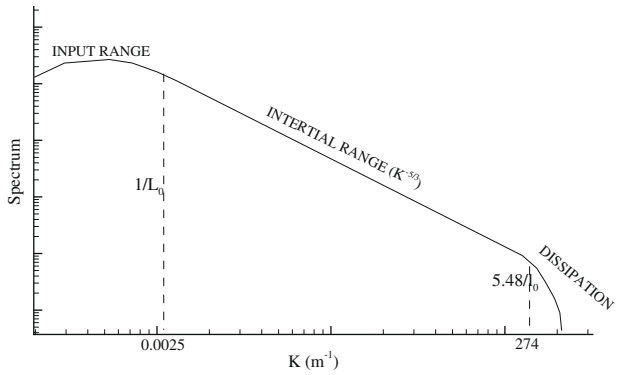

Fig. 1. Schematic of three-dimensional spectrum of the refractive index fluctuations. All important length scales are indicated in the figure for reference.

Table 1
Relevant length scales.

Length scales	Physical meaning
Outer scale of turbulence (L_0)	Length scale corresponding to the peak of the energy spectrum
Inner scale of turbulence (l_0)	Length scale indicating the beginning of the dissipation range
$\delta x, \delta y$ and δz	Grid resolution used in the LES simulation
$\Delta x, \Delta y$ and Δz	Grid resolution used for wave propagation simulation
l_x, l_y and l_z	Domain size used in the LES simulation
L_x, L_y and L_z	Domain size used for wave propagation simulation
$l_l = (\delta y \delta z)^{1/2}$	Length scale in the transverse plane for Eq. (12)
$l_w = (\Delta y \Delta z)^{1/2}$	Length scale in the transverse plane for Eq. (12)
L_{0H}	Average value of L_0 in the propagation domain
λ	Wavelength of the electromagnetic wave used

effect of inner and outer scales of the refractive index fluctuations, in the measured intensity variance, was studied. While field experiments are necessary to understand the over all mechanism, they are very expensive and do not give much insight into the problem as one get it using numerical simulations. Numerical simulations help in understanding the same with greater detail. In order to obtain the instantaneous data of atmospheric turbulence, using numerical simulation, the most commonly used technique among the boundary layer meteorologists is large-eddy simulation (LES) [10–14].

LES has been considerably developed over past 40 years for its use in turbulent flow simulations [15–17], which has been greatly facilitated by the increase in computing resources over time. In electromagnetic (EM) wave propagation modeling, the use of LES is restricted to the short range propagation of optical waves in turbulent media. It is commonly known as aero-optics [18–20], in which it is assumed that the propagation path is short enough to ignore any amplitude fluctuations. For long range propagation of EM waves, in which amplitude fluctuations also build up with the propagation distance, the use of LES is limited to the study of the behavior of refractive index structure function parameter C_n^2 [21,22].

To our knowledge, LES has never been used to provide the refractive index distribution directly into the three-dimensional (3D) wave propagation modeling. The reason obviously is the severe grid requirement for propagation modeling. The usual LES of atmospheric boundary layer provides turbulent refractivity on spatial scales down to a few tens of meters. These fields can be directly used for the propagation simulation of waves in HF [frequency: 3–30 MHz; wavelength (λ): 100–10 m] and VHF (10–1 m) bands but not wave of higher frequencies, for example, UHF (1 m to 100 mm) and SHF (10–1 mm) bands. The grid requirement for the propagation of these higher frequency waves can go much below 1 m, depending on the frequency. For a typical LES domain of $5 \times 5 \times 3$ km (3 km in the vertical direction), even a grid resolution of 1 m implies $5000 \times 5000 \times 3000$ points! Not to forget that some of these radio waves are used in television broadcasts or mobile phone communications in which the range of propagation extends up-to few hundred kilometers. Using a grid resolution, even of a meter, for such long distance propagation is simply impossible.

From the above discussion it seems that the use of LES, for long range radio wave propagation, is infeasible for two reasons:

(P1) Unavailability of very small sub-grid scale refractivity.
(P2) Requirement of long propagation distance, of the order of few hundreds of kilometers, when the usual LES domain size extend up-to only few kilometers.

The only attempt in this regard was made in [23], in which the authors used the LES data to study two-dimensional (2D) propagation of EM waves in gigahertz range. They used the Fourier based sub-grid regeneration technique of [24], to extend the resolved field of refractive index to higher grid resolution (hence P1 is resolved), and used it to study the propagation

factor of 0.263 GHz and 2 GHz waves over a distance of 120 km. They used the independent phase-screen technique, and generated the required number of phase-screens from their 5 × 5 × 2 km LES domain, to reach the desired propagation distance of 120 km (hence P2 is resolved). Although the method proposed in [23] is general, the sub-grid regeneration technique used by them requires use of 3D FFT for 3D propagation problems. 3D FFT of such huge amount of data consumes a lot of memory and require tremendous computational efforts – which makes their method unsuitable for the present work.

A new method is proposed in the present work, which is a natural improvement over the method of [23] in terms of computational cost and speed. In this method, instead of extending the resolved field of refractive index to higher grid resolution, we have used the same sub-grid regeneration technique to extend the phase fluctuations itself. This makes the present method much cheaper and faster than that of [23]. We will call this method a *hybrid phase-screen method* (HPSM) because it has phase contributions from: (i) resolved scales due to LES; and (ii) sub-grid scales due to statistical approach. The current work is organized in the following way. The next section is devoted for a brief discussion on the Fourier split-step algorithm followed by the development of the hybrid phase-screen approach. In Section 3, the usability of the new approach, in terms of both speed and accuracy, is shown with the help of numerical examples. Finally, we summarize the presented research in the conclusion.

2. Radio wave propagation in atmospheric turbulence via LES

For a wave field $\Phi = \psi(x,y,z)e^{-ik x}$ propagating in x direction, the amplitude ψ satisfies the parabolic approximation to the wave equation [25]

$$2ik\frac{\partial \psi}{\partial x} + \nabla_{\perp}^2\psi + 2k^2 n'\psi = 0, \tag{1}$$

where $k = 2\pi/\lambda$ is the wave number; $n' = n - \langle n\rangle$ is the fluctuating part of refractive index and $\nabla_{\perp}^2$ is Laplacian in the transverse direction. $\langle\rangle$ indicates spatial averaging. Eq. (1) can be solved numerically using the Fourier split-step method [26] for its accuracy and speed. The split-step solution of ψ at $x + \Delta x$ is given as:

$$\psi(x+\Delta x, y, z) = e^{i\phi}F^{-1}[\psi(x, K_{\perp})e^{-iK_{\perp}^2\Delta x/(2k)}] \tag{2}$$

where, F^{-1} indicates the 2D inverse Fourier transform in the plane perpendicular the propagation direction (transverse plane) and $\psi(x,K)$ is the Fourier transform of ψ at x. $K_{\perp} = \left(k_y^2 + k_z^2\right)^{1/2}$ is the wave number in the transverse plane. The phase ϕ in Eq. (2) is related to the refractive index fluctuations n' of the medium through:

$$\phi(x,y,z) = k\int_x^{x+\Delta x} n'(x,y,z)\,dx. \tag{3}$$

In practice, unless the turbulent refractivity is already available, Eq. (3) is not used directly to estimate the phase because of the high computational cost involved in it. The usual approach is to use SPSM, which allows one to directly calculate phase, without using Eq. (3). The details of the method can be found in [4]. This method is based on the Markov's approximation [27,28] according to which a continuous random medium can be decomposed into a series of statistically independent phase-screens. In SPSM, the 2D phase spectrum $\hat{\phi}$ of each screen is related to the 3D refractive index spectrum $\hat{n}$ through:

$$\hat{\phi}(k_y, k_z) = 2\pi k^2 \Delta x \hat{n}(k_x = 0, k_y, k_z). \tag{4}$$

This relationship is based on the assumption that the correlation length of the irregularities in the medium is less than the separation (Δx) between the screens. This makes these screens statistically uncorrelated and hence allows one to take larger Δx. The phase is then generated using the following discrete version of 2D inverse Fourier transform:

$$\phi(j\Delta y, l\Delta z) = \sum_{n=0}^{N_y}\sum_{m=0}^{N_z}[a(n,m) + ib(n,m)]\exp[2\pi i(jn/N_y + lm/N_z)] \tag{5}$$

where, $i^2 = -1$; Δy and Δz are the grid spacing in the phase-screen; N_y and N_z are number of points in the respective directions; and $a(n,m)$ and $b(n,m)$ are the zero-mean Gaussian uncorrelated random numbers with

$$\langle a^2(n,m)\rangle = \langle b^2(n,m)\rangle = \Delta k_y \Delta k_z \hat{\phi}(n\Delta k_y, m\Delta k_z). \tag{6}$$

Here, $\langle\rangle$ denotes ensemble average and $\Delta k_y = 2\pi/(N_y\Delta y)$ and $\Delta k_z = 2\pi/(N_z\Delta z)$ are the grid size of k_y and k_z in the spectral plane. The phase spectrum $\hat{\phi}$ is obtained from Eq. (4) using a suitable refractive index spectrum.

The limitation of using SPSM is already mentioned in the introduction. Our aim in the present work is to circumvent this limitation using the resolved scales from LES. Therefore, for HPSM we re-write the phase in Eq. (3) as:

$$\phi(x,y,z) = k\int_x^{x+\Delta x} n'(x,y,z)dx = k\int_x^{x+\Delta x} n'_r(x,y,z)dx + k\int_x^{x+\Delta x} n'_s(x,y,z)dx = \phi_r(x,y,z) + \phi_s(x,y,z). \tag{7}$$

Here, n'_r is the resolved scale part and n'_s is the sub-grid scale part of total refractive index fluctuation n'. Same with $\phi_r(x,y,z)$ and $\phi_s(x,y,z)$. Because we already have n'_r from the LES simulation, it will be advantageous to calculate $\phi_r(x,y,z)$ by direct integration of n'_r. This part of the method is same as that of [23]. The difference lies in estimating the sub-grid phase ϕ_s(x,y,z). If we chose to use the method of [23], in our 3D problem, then we have to first calculate n'_s using $\hat{n}$ in 3D version of Eq. (6), and then perform the 3D version of Eq. (5). The 3D operation of Eq. (5), makes their method more costlier than ours, in which, $\phi_s(x,y,z)$ is calculated using Eq. (4) together with Eqs. (5) and (6), involving only 2D FFT operations. The methodology to estimate ϕ_r and ϕ_s is described next.

2.1. Resolved scale phase: $\phi_r(x,y,z)$

In LES the filtered version of the Navier–Stokes equations are solved to provide full 3D turbulent fields of the most energetic (resolved) scales. These resolved scale variables are identified with a subscript r in the present text. Therefore, we can write the total refractive index as

$$n(x,y,z,t) = n_r(x,y,z,t) + n_s(x,y,z,t), \tag{8}$$

and total refractive index fluctuations $(n' = n - \langle n \rangle)$ as

$$n'(x,y,z,t) = n'_r(x,y,z,t) + n'_s(x,y,z,t). \tag{9}$$

Here, n_r is the resolved scale part and n_s is the sub-grid part of total refractive index n. $n'_r = n_r - \langle n_r \rangle$ is the fluctuation in the resolved scale and $n'_s = n_s$ is the fluctuation in the sub-grid part of the total refractive index fluctuation n'. $\langle\rangle$ indicates spatial averaging in the homogeneous (X–Y) plane. The general purpose finite-volume code, *code_Saturne* [29], was used to perform the LES of the shallow-cumulus convection over a domain of length $(l_x \times l_y \times l_z) = (5 \times 5 \times 3\ \text{km})$. The grid used in the present simulation is uniform in all the directions, with $\delta x = \delta y = 62.5$ m and $\delta z = 30$ m. Here, $\delta x, \delta y$, and δz are the LES grid resolution in the stream-wise, span-wise, and in the vertical directions, respectively. The case of shallow-cumulus cloud convection is well documented in the literature, both experimentally and numerically, and can be found in [30–32] and the references there in.

The code we have used is developed by the scientists in *Electricite de France* and is well assessed for many application of turbulent flows and atmospheric flows. It is a finite-volume code using collocated grids. The spatial discretization used in the current research is second-order central differencing and the temporal discretization is second-order implicit. Periodic boundary condition is used in the X–Y plane and other details of the formulation, schemes, and the obtained results are given in [33,29]. The LES results have been verified for their grid convergence behavior also, by using grid resolution more than twice used in this paper, and is reported somewhere else. For radio waves, n is related to the state variables by the following expression [34]:

$$n = 1 + n_d + n_w \tag{10}$$

where,

$$n_d = \left(77.6\frac{p}{T} - 124.9\frac{pq}{T}\right) \times 10^{-6}$$
$$n_w = \left(115.9\frac{pq}{T} + 6.0356 \times 10^5 \frac{pq}{T^2}\right) \times 10^{-6}. \tag{11}$$

Here, p is the total instantaneous pressure in hectopascal; q is the specific humidity; and T is the absolute temperature (in Kelvin). n_d and n_w are the contributions due to the dry air and water vapor, respectively. With the assumption that the same expression holds for n_r also (up-to first order accuracy), $n'_r = n_r - \langle n_r \rangle$ can be estimated using the LES data. The instantaneous distribution of n'_r, as obtained the LES run, is shown in Fig. 2. The figure shows iso-surfaces corresponding to $n'_r = -3 \times 10^{-6}$ (dark) and $n'_r = 3 \times 10^{-6}$ (bright). These large scale refractive index fluctuations, as seen in the figure, are dominant only till $z \sim 1500$ m. Further high in the atmosphere, these fluctuations tend to decay due to the presence of the stable inversion layer on top of it. Once n'_r is obtained, ϕ_r is calculated by performing the integration in Eq. (7).

It is to be noted that n'_r is located on the grid points corresponding to the LES simulation, which usually is much coarser than the grid resolution required for the propagation problem. Independent phase-screens allow one to take $\Delta x > \delta x$, but, Δy and Δz has to be much finer than δy and δz, to capture the small scale phase fluctuations. Therefore, some kind of interpolation will be required for n'_r, in the transverse plane, before performing the integration. This interpolation is just a numerical adjustment to provide a smooth variation of the phase over the entire phase-screen. Cubic-spline interpolation is used in the present simulation.

2.2. Sub-grid scale phase: $\phi_s(x,y,z)$

In the usual SPSM, the phase spectrum in Eq. (4) is assumed to be valid at all spatial wave numbers. In HPSM, because we already have ϕ_r from the LES data, Eq. (4) is now required only for the sub-grid scales. If we denote that length scales, corresponding to LES grid size and the wave propagation grid size, in the transverse plane, respectively as $l_l = (\delta y \delta z)^{1/2}$ and $l_w = (\Delta y \Delta z)^{1/2}$, then the spatial range of the desired phase-spectra reduces to:

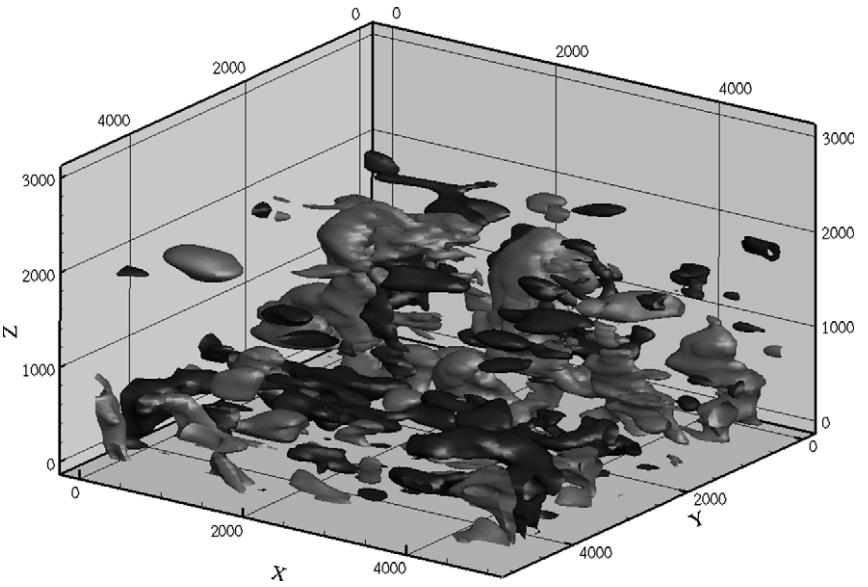

Fig. 2. Iso-surfaces of the resolved part of refractive index fluctuations, $n'_r = -3 \times 10^{-6}$ (dark) and $n'_r = 3 \times 10^{-6}$ (bright), as obtained using the LES results in Eq. (10).

$$\hat{\phi}(K_\perp) = \begin{cases} 2\pi\kappa^2 \Delta x \hat{n}(k_x = 0, K_\perp) & \text{if } \frac{\pi}{l_w} > K_\perp > \frac{\pi}{l_l}, \\ 0 & \text{otherwise.} \end{cases} \tag{12}$$

The next step is to generate 2D array of zero-mean Gaussian random number and follow the Eqs. (5) and (6) to get $\phi_s(y,z)$, at a given location in x, corresponding to the screen position. Refractive index spectrum plays a vital role in Eq. (12) and in Eq. (4), and one should be very careful in selecting it. In the present simulation, we have used the large scale part of von Karman spectrum, together with the dissipation range formulation of [35] to get:

$$\hat{n}(K,z) = 0.0330054 C_n^2(z)(K^2 + 1/L_0^2(z))^{-11/6} f[K l_0(z)]. \tag{13}$$

Here, $K = \left(k_x^2 + k_y^2 + k_z^2\right)^{1/2}$ is the magnitude of the three-dimensional wave vector and $f(x) = (1.0 + 0.70937x + 2.8235x^2 - 0.28086x^3 + 0.08277x^4)e^{-1.109x}$ shows the effect of the inner scale in the dissipation range [35]. It is to be noted that the term corresponding to large scales $(1/L_0^2(z))$, in Eq. (13), is only required for SPSM in Eq. (4). For HPSM, this effect is already included in ϕ_r due to the resolved scales of LES simulation, and hence is dropped when used in Eq. (12).

Direct evaluation of L_0 using LES results is not trivial and the only available formula, due to Eq. (3.29") of [28], was found to give underestimated values during our preliminary runs. It is for this reason, for the present work, L_0 values are obtained using the 1D horizontally averaged spectrum of specific humidity fluctuations $(\mathrm{E}(k_x))$. These 1D spectra, at some representative altitudes, are shown in Fig. 3; along with the $k_x^{-5/3}$ slope for reference. The relationship between L_0 and $\mathrm{E}(k_x)$ is given by Pope [36]:

$$L_0 = \frac{\pi}{12\langle q'^2 \rangle} \int_0^\infty \frac{E(k_x)}{k_x}\, dk_x \tag{14}$$

where, $\langle q'^2 \rangle$ is the mean specific humidity variance as obtained from the LES simulation. The factor of 12 in the denominator of Eq. (14) comes from the discussion on page 242 of [36].

The values of L_0 hence obtained are shown in Fig. 4, along with $C_n^2(z)$ and $l_0(z)$, as calculated from the LES simulation. The evaluation method and the validity of C_n^2 and l_0 are discussed in [33]. It is important to note that the flow is in-homogeneous in the vertical (Z) direction, and this effect has to be included in the phase-screens. While ϕ_r readily includes this effect due to the LES results; this effect is included in ϕ_s through the vertical dependency of $C_n^2(z), L_0(z)$ and $l_0(z)$.

Sample phase-screens, as obtained from the proposed approach (top frame) and SPSM (bottom frame), are shown in Fig. 5. $\phi_r(y,z)$ is obtained after integrating over $\Delta x = 1$ km. Both these screens are obtained at the same location in X. The presence of large scale coherent structures in Fig. 5(a) indicates the effect of the correlation at the larger scales, which is correctly captured with HPSM. This information is completely missing in Fig. 5(b) due to SPSM. The benefit of our approach lies in using these large scale information, as obtained from the LES simulation, to get correct statistical description at larger scales and to get the correlation effects at these scales. This will help in getting better understanding of the propagation effects in atmospheric turbulence. The randomness in the distribution of phase across the screen is proportional to the amount

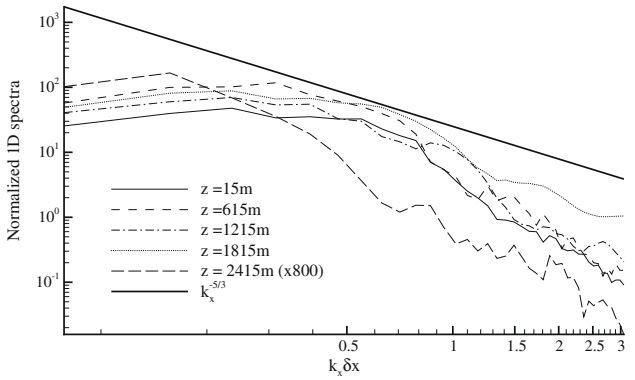

Fig. 3. Horizontally averaged one-dimensional spectra of specific humidity fluctuations, after normalization, is shown at indicated altitudes. Note that the spectrum at $z = 2415$ m is multiplied by 800.

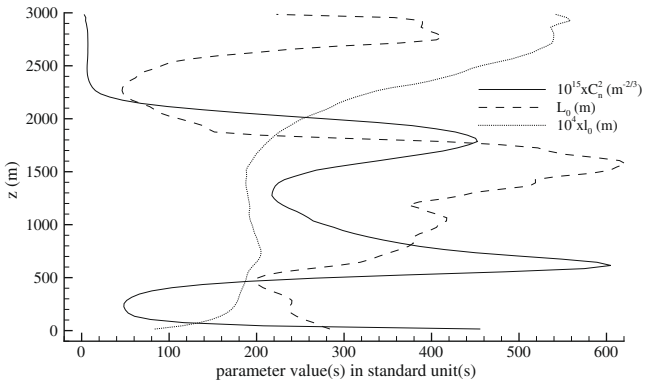

Fig. 4. Vertical profile of l_0, L_0, and C_n^2 as obtained from the LES of shallow-cumulus convective boundary layer. Note the multiplicative constants in the legend.

of distortion it imposes on the incident wave front. Clearly, the strong randomness in Fig. 5(b) is indicative of the strong distortion of the incident wave front due to SPSM.

2.3. Turbulent refractivity beyond the LES computational domain

Large domain size requirement, for the propagation study of the radio waves, makes our task even more difficult. It, of course, is infeasible to perform LES of atmospheric boundary layer over a domain of length, say, 200 km while keeping the same grid resolution. This situation was beautifully handled in [23], for their 2D propagation problem, by using the longitudinal slices from one of the homogeneous directions of their LES domain. These longitudinal slices were then used to generate the desired number of uncorrelated 1D phase-screens.

Unlike [23], we need 2D phase-screens for our 3D propagation simulation. Extending their idea for our problem is more involved, the details of which is explained below. Let the size of the LES domain be $l_x \times l_y \times l_z$ in X, Y and Z-directions, respectively. As already mentioned, X and Y correspond to the homogeneous directions. Let the corresponding size of the propagation domain be $L_x \times L_y \times L_z$, for L_x as the length in the direction of propagation and $L_y \times L_z$ as the size of the 2D phase-screen. In general, for practical purposes, $L_x > l_x, L_y < l_y$ and $L_z < l_z$.

It is clear that frm a LES domain of length l_x, the maximum number of phase-screens that we can get is $\frac{l_x}{\delta x}$ (for $\Delta x = \delta x$), and the minimum is 1 (for $\Delta x = l_x$). This count can be further increased if we notice the homogeneity in the Y direction. Because $L_y < l_y$, we can generate l_y/L_y times more phase-screens by simply shifting in Y-direction. Therefore, the total number of phase-screens, ns, that we can get from a single LES domain is:

$$\frac{l_y}{L_y} \leqslant ns \leqslant \frac{l_x}{\delta x}\frac{l_y}{L_y}.$$

The exact number will depend on the desired Δx. In the case we need total number of phase-screen such that $\mathrm{NS}(= L_x/\Delta x) > ns$, the remaining $\mathrm{NS} - ns$ screens can be generated from LES results collected at uncorrelated time instant(s).

In the present simulation, LES results were stored at every $\tau = l_x/\langle u \rangle$ (after the flow became statistically steady), to ensure the uncorrelation mentioned above. This is just a rough rule based on the assumption that τ is the time taken by the disturbances to make one complete cycle of the LES domain. Here, $\langle u \rangle$ is the speed in the X-direction, calculated by averaging over the whole computational domain for a long duration of time. It is important to note that screens thus generated should be used randomly to avoid any kind of correlation effect between them. Presence of any regular pattern, between successive screens, can cause accumulation of energy at that particular scale, leading to spurious results.

3. Implementation algorithm and numerical examples

Once the LES fields are obtained, the implementation of HPSM is simple and is provided below in a composite manner:

(A) Fix the phase-screen size required for the propagation simulation. Let $L_y \times L_z$ be the size of the phase-screen divided into $N_y \times N_z$ number of equal parts, respectively.
(B) Chose its location in the LES domain (desired vertical location) and calculate n'_r in this part ($l_x \times L_y \times L_z$) using Eq. (10). Interpolate n'_r from LES grid to $N_y \times N_z$ points in the transverse direction.
(C) Estimate the number of phase-screens (ns) that can be generated from one LES domain, for the desired Δx, following the discussions in Section 2.3. Calculate ϕ_r for these screens using n'_r obtained in (B) by performing the integral in Eq. (7).
(D) Calculate ϕ_s at all ns phase-screens using Eq. (12) in Eqs. 6 and 5.
(E) Total phase at each screen is then obtained as $\phi_r + \phi_s$.

In case more screens are required, steps (A)–(E) can be repeated for LES results collected at uncorrelated time instant(s), as discussed in the previous section.

We can notice that the algorithm is almost the same as the usual SPSM method. Only difference is in step (B), in performing the interpolation, and in step (C), in performing the integral. Effect of these two extra steps in the computational speed of HPSM, is shown through the ratio $r = \frac{\text{time elapsed in HPSM}}{\text{time elapsed in SPSM}}$ in Fig. 6. Fig. 6(a) shows the variation of r, with the number of phase-screens (NS), when the number of points in each screen is kept constant at $N_y = N_z = 128$. As the number of phase-screen increases, the ratio starts to come down, slowly, from $r = 4$ to a nearly constant value of $r = 1.42$. The results in Fig. 6(b) are obtained by increasing the value of N_y (=N_z) for NS = 48. This time, although the ratio started with a very high value of $r = 12$, the fall in r is very rapid and it immediately comes down a saturation value of $r = 1.08$. These results clearly

establish that the present method is only little slower than SPSM, for the real time problems, in which the number of points are usually on the higher side.

It has been already mentioned that the advantage of the present approach, over SPSM, lies in capturing the effect of the scales larger than L_0. Obviously, large scale effects are more important for larger waves. In our present exercise, we have chosen two plane waves of unity amplitude: small wave ($\lambda = 0.005$ m) and large wave ($\lambda = 0.01$ m), to demonstrate the same through the variation of normalized intensity $I_N(x,z)$ and normalized intensity variance $\sigma_I^2(x)$ with propagation distance x. The obtained results have been compared with those from SPSM. The normalized intensity I_N, where

$$I_N(x,z) = \frac{\langle \psi(x,y,z)\psi^*(x,y,z)\rangle}{\langle \psi(0,y,z)\psi^*(0,y,z)\rangle} \tag{15}$$

is calculated for different values of x and z as indicated. The angular bracket $\langle\rangle$ here indicates averaging over y and $\psi^*(x,y,z)$ is complex conjugate of the wave amplitude ψ.

Normalized intensity variance is defined as:

$$\sigma_I^2(x) = \frac{\langle I(x)^2\rangle}{\langle I(x)\rangle^2} - 1, \tag{16}$$

where $I(x)$ is intensity of the incident wave at x and $\langle\rangle$ denotes averaging in the transverse (Y–Z)-plane. Because of the inherent periodicity involved with the Fourier Split-step method, one needs to be careful with the result near the screen boundaries. For this reason, only center half of the total screen size is used to get $\langle I(x)\rangle$ for a particular screen.

The common practice in wave propagation research is to plot σ_I^2 with respect to the low scattering formulation of σ_I^2, as obtained by Rytov's approximation [4,27]. For pure Kolmogorov spectra, the Rytov's approximation for normalized intensity variance of plane wave is identified as β^2 and is given as:

$$\beta^2 = 1.23\overline{C}_n^2 \kappa^{7/6} x^{11/6}. \tag{17}$$

Here, x, as before, is the propagation distance; and $\overline{C}_n^2$ is the average value of C_n^2 across the phase-screen in our simulation and its value is given in Table 2. All our simulation results below are performed for propagation length corresponding to $\beta^2 = 15$ and the results for σ_I^2 are plotted against β^2. It is to be noted that for long distance propagation problems, one should ideally account for the effect of the earth's curvature on the turbulent refractivity. We have not considered it in our simulations because our aim here is to compare the two methods for the same input conditions.

To get a statistically converged result, one needs to run the whole simulation a number of times for different set of random numbers. One such run of the wave, starting from the first screen till the final screen, is counted as a single realization. The final result for σ_I^2 and $I_N(x,z)$ is then obtained after averaging over these realizations. Convergence study is made to find

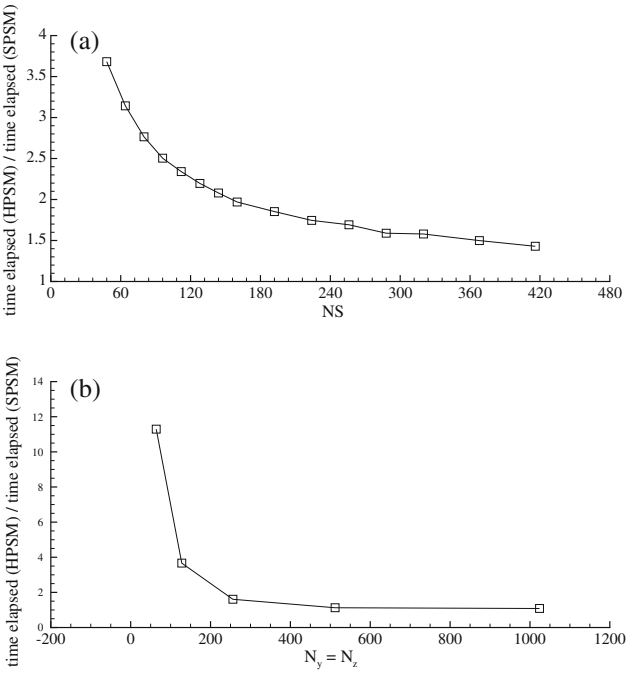

Fig. 6. Comparison of the computational speed of HPSM and SPSM when: (a) $N_y = N_z = 128$ and NS is increasing; and (b) NS = 48 and $N_y (= (N_z)$ is increasing.

out the minimum number of realizations required, to get statistically converged results, for both the methods. The obtained results are shown in Fig. 7. The figure clearly shows that the minimum number of realizations required for HPSM and SPSM are 10 and 30, respectively.

It is important to realize that the only limitation of HPSM is that the screens generated are not truly statistically uncorrelated, as one gets in SPSM. It is because SPSM is based on the assumption that Δx is much larger than the correlation length in the propagation direction, which is not the case with HPSM. For HPSM, depending on the flow conditions, the horizontal correlation length can be as large as the length of the LES domain (l_x) itself, which equals the maximum allowable value of Δx. Randomizing the screens, as discussed in the previous section, does help in relaxing the situation, but it does not remove it completely. Therefore, one should be particularly careful in choosing the number of screens (or Δx) for HPSM. A very large value of Δx, and randomization, can make the successive screens independent, but, it will then increase the error in the Fourier split-step method itself [6,26].

From the discussion above it is clear that the results due to HPSM are sensitive to the number of screens. This is shown in Fig. 8, for the case-1 of Table 2, for different values of NS. Based on the shown results and our experience, we have observed that $1.5L_{0H} < \Delta x < 3.5L_{0H}$ is a good compromise between the two sources of error mentioned above. Here, L_{0H} is the value of L_0 averaged over the height of the propagation domain.

The size of the screen ($L_y \times L_z$) and the number of points ($N_y \times N_z$) are also very important parameters, and they should to be chosen carefully depending on the size of the Fresnel zone $r_f = (Propagationlength/\kappa)^{1/2}$, for wave number κ [6]. Effect of change in $N_y \times N_z$, for case-1 in Table 2, is shown in Fig. 9. The figure does not clearly reveal the optimum number of points needed for the simulation. For the reason of greater computing speed, we have decided to use $N_y = N_z = 1024$ for our remaining simulations. The value of other parameters, relevant for propagation study, is provided in Table 2.

Table 2
Simulation parameters for case under study.

Parameters	Case-1 ($\lambda = 0.005$ m)	Case-2 ($\lambda = 0.01$ m)
Propagation length L_x (km)	255	500
NS	255	500
$L_z \times L_y (m^2)$	500×500	950×950
$N_y = N_z$	1024	1024
$\overline{C_n^2}$	0.37×10^{-12}	0.24×10^{-12}
β^2	15	15

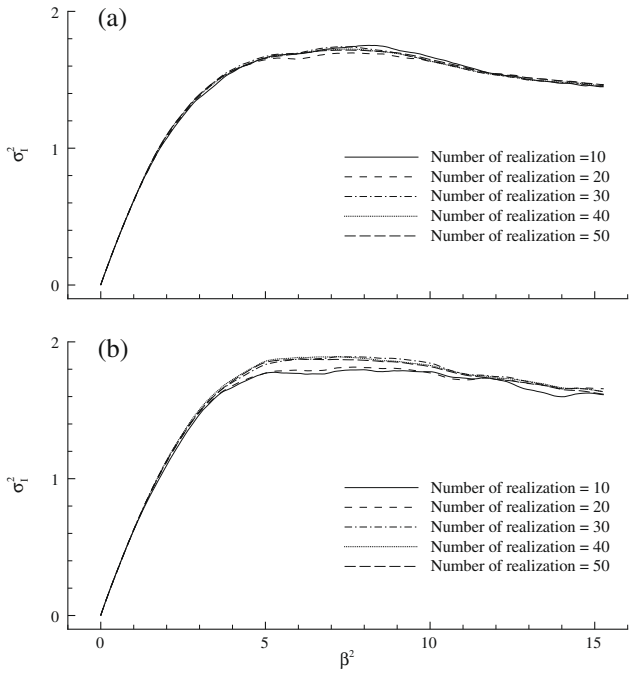

Fig. 7. Convergence study of: (a) HPSM; and (b) SPSM, for the case-1 in Table 2, for different number of realizations.

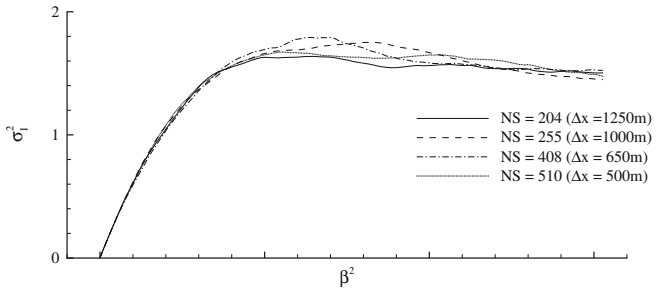

Fig. 8. Convergence study of HPSM, for the case-1 in Table 2, for change in the number of phase-screens (NS).

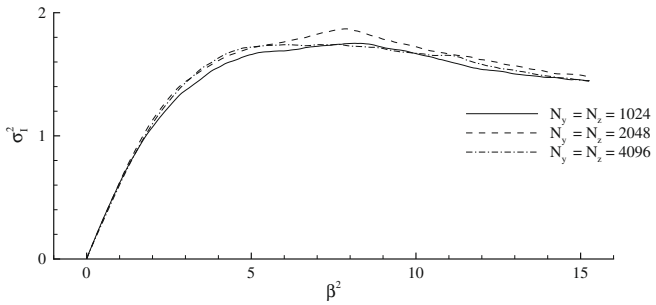

Fig. 9. Convergence study of HPSM, for the case-1 in Table 2, for change in the number of points per screen.

Next we have compared σ_I^2, from both the methods, in Fig. 10. Fig. 10(a) shows the variation of σ_I^2 with propagation distance for the case-1 of Table 2. The difference between the two curves show the effect of scales larger than L_0, through ϕ_r, which are correctly captured in HPSM and not in SPSM. It is already known that scattering is more if the wavelength of the incident wave is comparable to the size of the turbulent scale [27]. This implies that for a given turbulent medium, the effect of scattering, due to large turbulent scales ($> L_0$), will be more in case-2 (large λ) than in case-1. This is because the wave in case-2 is more close to the scales $> L_0$ than the wave in case-1. It is clearly visible in Fig. 10(b), where σ_I^2 is shown for case-2. These two figures clearly indicate that the effect of ϕ_r is very pronounced in the region of strong scattering ($\sigma_I^2 > 1$), which can not be ignored.

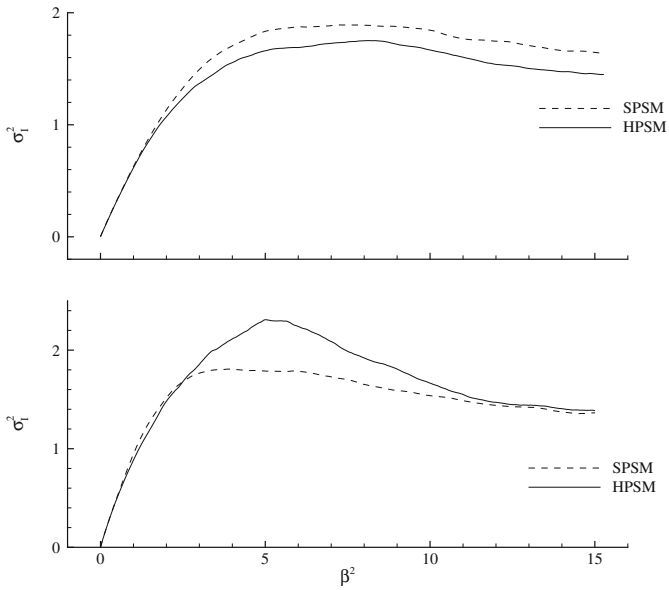

Fig. 10. Normalized intensity variance vs. β^2 for: (a) case-1 (NS = 510); and (b) case-2 (NS = 1000) in Table 2, using indicated methods.

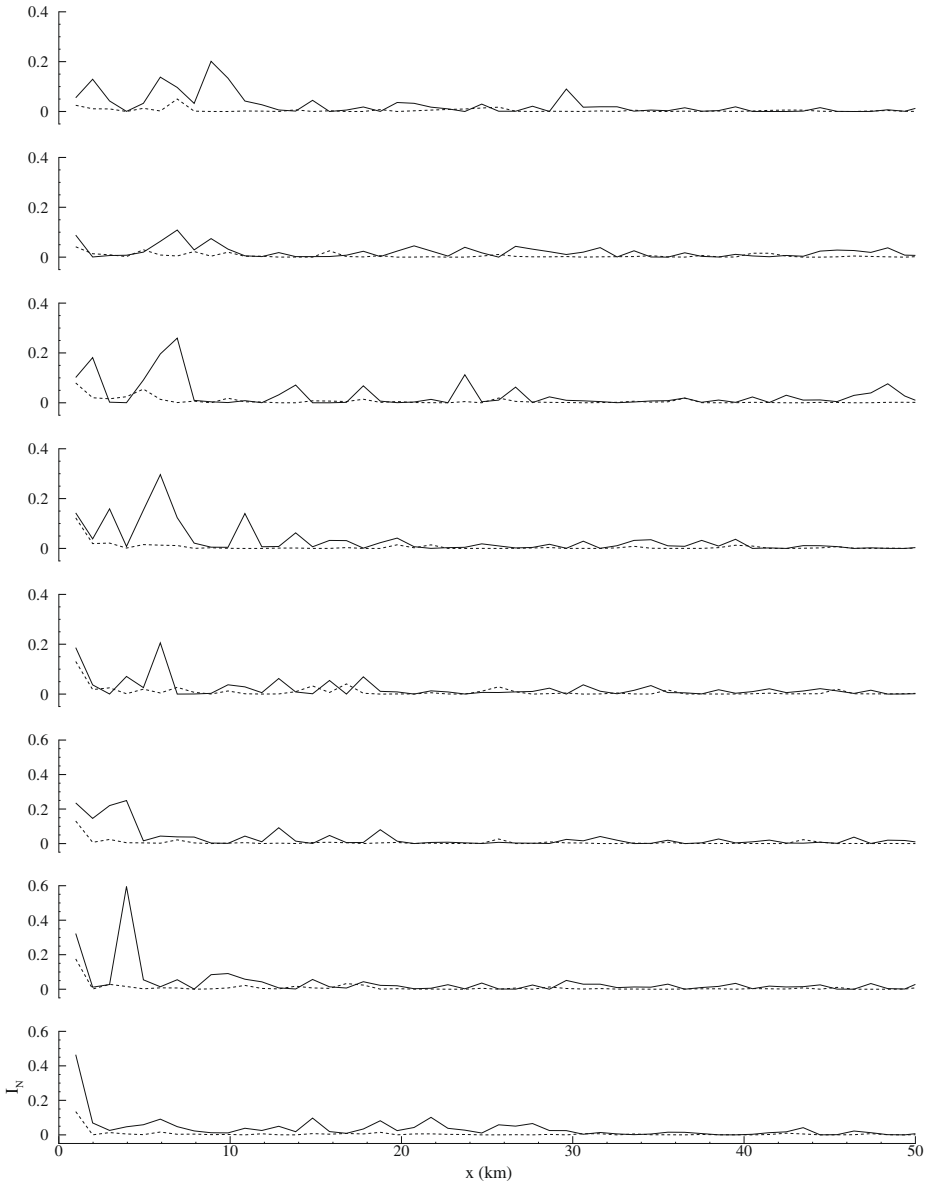

Fig. 11. Variation of normalized intensity $I_N(x,z)$ with x, for case-1 in Table 2, using HPSM (solid line) and SPSM (dotted line). Results are shown at different altitudes in increasing order (from top to bottom). Note that I_N is obtained after averaging over 10 different realizations for all values of y.

Higher moments of the wave field, for example σ_I^2, show the reduced effect of the differences between the two methods. This difference is more distinctly visible in the spatial variation of $I_N(x,z)$, shown next. The variation of I_N with distance, for the case-1, at different altitudes (z), is shown in Fig. 11, along with the results from SPSM. The difference in the two approach is clearly visible in the figure. It is important to note here that the decay in intensity is very rapid with SPSM than it is with HPSM. It is due to the strong randomness in the phase-screen generated using SPSM (see Fig. 5). At longer distances, the difference between the two is greatly reduced and both of them approach to their respective saturation values in a steady manner. As expected, the variation in I_N, for $\lambda = 0.01$m, show even larger difference between the two approach. It is shown in Fig. 12. Interesting thing to note in this figure is that the intensity, at the very first screen, due to these two methods show a very large difference. While $I_N \approx 0.6$ (at first screen) for SPSM, it is around 0.05 for HPSM. This large difference can be attributed to the large scale effects correctly captured in HPSM. Unlike case-1, the differences between HPSM and SPSM are quite prominent for case-2, even at larger distances. From the above discussions we conclude that the differences between SPSM and HPSM keep on increasing with wavelength and therefore SPSM is not suitable for the waves in radio region.

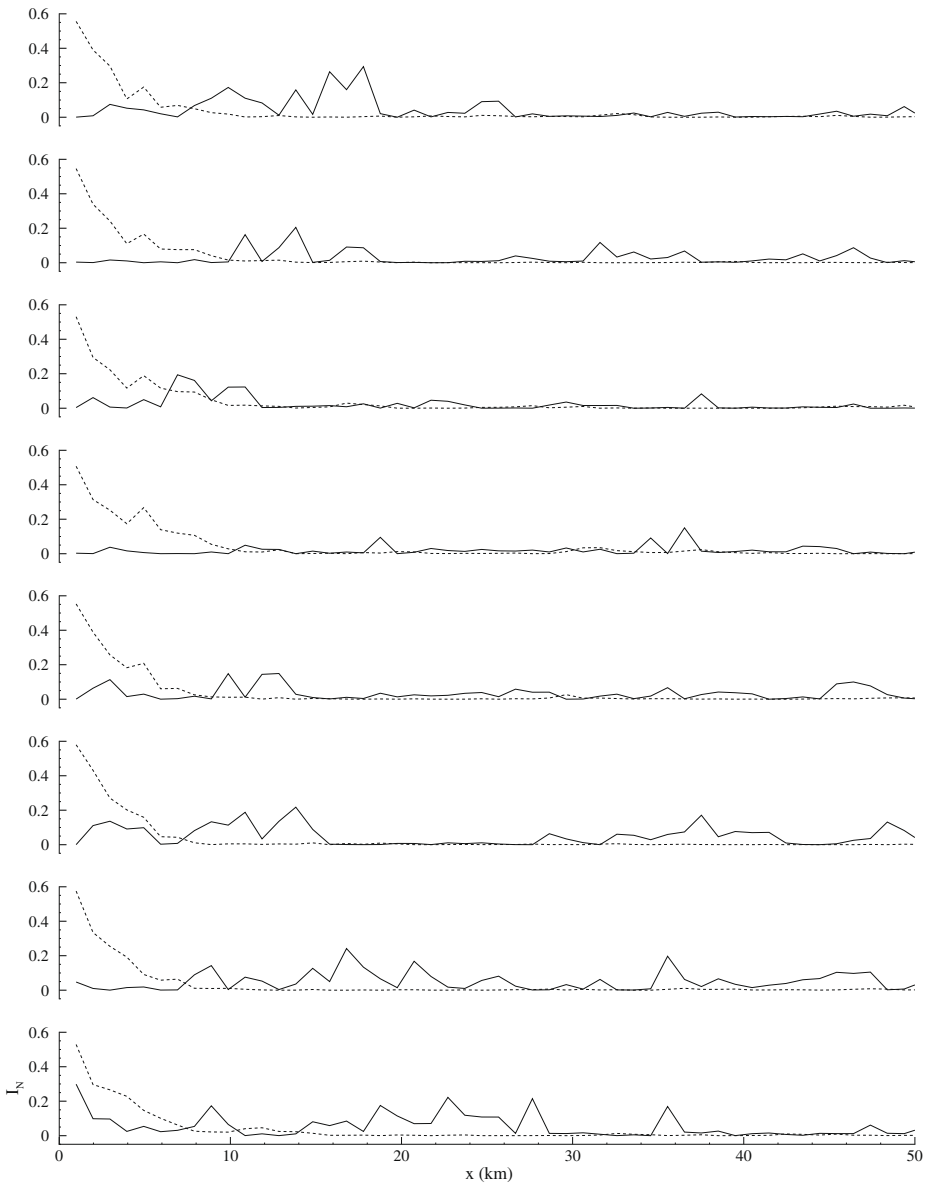

Fig. 12. Same as Fig. 11 for case-2 in Table 2.

4. Conclusions

Large-eddy simulation has its use in many applications of both scientific and engineering interests. A method (HPSM) is proposed that widens its range of applicability even more and allows one to use LES data in radio wave propagation modeling in atmospheric turbulence. The proposed method is more accurate, than the most commonly used (statistical) independent phase-screen method (SPSM), because it correctly captures the large scale effects using the resolved scales data from LES. These effects are captured through correct modeling of resolved phase term ϕ_r in Section 2.1.

It is shown here that instead of generating sub-grid scale refractivity, it is more advantageous to directly generate the sub-grid scale phase fluctuations, using the Eq. (12). This avoids the use of costly 3D FFT operations – making the present method as the only available technique for use of LES fields in radio wave propagation. A simple technique has been proposed in Section 2.3, to generate the required number of independent phase-screens, using LES simulated data. The computational cost involved in the HPSM is almost the same as the SPSM provided the LES field is already obtained.

The usability and advantage of HPSM is demonstrated through propagation simulation of plane waves of wavelength $\lambda = 0.005$ m and $\lambda = 0.01$ m. It has been shown that the large scale effects play very dominant role in the region of strong

scattering. These effects are more pronounced for larger waves and SPSM fails to correctly predict the intensity and its variance in that situation.

Acknowledgment

We would like to thank the anonymous reviewer who read the manuscript very thoroughly and made valuable comments. His suggestions and comments were very helpful in improving the quality of the present work.

References

[1] A.E. Barrios, A terrain parabolic equation model for propagation in troposphere, IEEE Trans. Antennas Propagat. 42 (1994) 90–98.
[2] G.D. Dockery, Modelling electromagnetic wave propagation in the troposphere using parabolic equation, IEEE Trans. Antennas Propagat. 36 (10) (1988) 1464–1470.
[3] S.W. Marcus, A hybrid (finite difference-surface Green's function) method for computing transmission losses in an inhomogeneous atmosphere over irregular terrain, IEEE Trans. Antennas Propagat. 40 (12) (1992) 1451–1458.
[4] J.M. Martin, S.M. Flatte, Intensity images and statistics from numerical simulation of wave propagation in 3D random media, Appl. Opt. 27 (11) (1988) 2111–2126.
[5] D.L. Knepp, Multiple phase-screen calculation of the temporal behavior of stochastic waves, Proc. IEEE 71 (6) (1983) 722–737.
[6] W.A. Coles, J.P. Filice, R.G. Frehlich, M. Yadlowsky, Simulation of wave propagation in three-dimensional random media, Appl. Opt. 34 (12) (1995) 2089–2101.
[7] R. Frehlich, Simulation of laser propagation in a turbulent atmosphere, Appl. Opt. 39 (3) (2000) 393–397.
[8] A. Consortini, F. Cochettti, J.H. Churnside, R.J. Hill, Inner-scale effect on irradiance variance measured for weak-to-strong atmospheric scintillation, J. Opt. Soc. Am. A 10 (11) (1993) 2354–2362.
[9] R.S. Cole, K.L. Ho, N.D. Mavrokoukoulakis, The effect of the outer scale of turbulence and wavelength on scintillation fading at millimeter wavelengths, IEEE Trans. Antennas Propagat. 26 (5) (1978) 712–715.
[10] J.W. Deardorff, Numerical investigation of neutral and unstable planetary boundary layers, J. Atmos. Sci. 29 (1972) 91–115.
[11] C.H. Moeng, A large-eddy-simulation model for the study of planetary boundary layer turbulence, J. Atmos. Sci. 41 (1984) 2052–2062.
[12] H. Schmidt, U. Schumann, Coherent structure of the convective boundary layer derived from large-eddy simulations, J. Fluid Mech. 200 (1989) 511–562.
[13] F. Porte-Agel, C. Meneveau, M.B. Parlange, A scale-dependent dynamic model for large-eddy simulation: application to a neutral atmospheric boundary layer, J. Fluid Mech. 415 (2000) 261–284.
[14] D. Drikakis, Advances in turbulent flow computations using high-resolution methods, Prog. Aero. Sci. 39 (2003) 405–424.
[15] P. Sagaut, Large-eddy Simulation for Incompressible Flows – An Introduction, third ed., Springer Verlag, Scientific Computation Series, 2005.
[16] B.J. Geurts, Elements of Direct and Large-eddy Simulation, Edwards, 2004.
[17] D. Drikakis, W. Rider, High Resolution Methods for Incompressible and Low Speed Flows, Springer, 2005.
[18] A. Mani, M. Wang, P. Moin, Resolution requirements for aero-optical simulations, J. Comput. Phys. 227 (21) (2008) 9008–9020.
[19] A. Mani, M. Wang, P. Moin, Statistical description of the free-space propagation of highly aberrated optical beams, J. Opt. Soc. Am. A 23 (2006) 3027–3035.
[20] E. Tromeur, E. Garnier, P. Sagaut, C. Basdevant, Large eddy simulations of aero-optical effects in a turbulent boundary layer, J. Turbulence 4 (005) (2003) 1.
[21] S.D. Burk, Refractive index structure parameters: time-dependent calculations using a numerical boundary-layer model, J. Appl. Meteorol. 19 (1979) 562–576.
[22] L.J. Peltier, J.C. Wyngaard, Structure-function parameters in the convective boundary layer from large-eddy simulation, J. Atmos. Sci. 52 (21) (1995) 3641–3660.
[23] K.E. Gilbert, X. Di, S. Khanna, M.J. Otte, J.C. Wyngaard, Electromagnetic wave propagation through simulated atmospheric refractivity fields, Radio Sci. 34 (6) (1999) 1413–1435.
[24] R.H. Kraichnan, Isotropic turbulence and intertial-range structure, Phys. Fluids 9 (9) (1966) 1728–1752.
[25] A.N. Monin, A.M. Yaglom, Statistical Fluid Mechanics II, MIT Press, Cambridge, 1971.
[26] J.R. Kuttler, G.D. Dockery, Theoretical description of the parabolic approximation/Fourier split-step method of representing electromagnetic propagation in the troposphere, Radio Sci. 26 (2) (1991) 381–393.
[27] A. Ishimaru, Wave Propagation and Scattering in Random Media, Oxford University Press, Oxford and IEEE Press, New York, 1997.
[28] V.I. Tatarski, Wave Propagation in a Turbulent Medium, Dover Publication, Inc., New York, 1967 (Translated from the Russian by R.A. Silverman).
[29] F. Archambeau, N. Mechioua, M. Sakiz, *Code_Saturne*: a finite volume code for the computation of turbulent incompressible flows- industrial applications, Int. J. Finite Vol. 1 (2004) 1–62.
[30] J.W.M. Cujipers, P.G. Duynkerke, Large eddy simulation of trade wind cumulus clouds, J. Atmos. Sci. 50 (23) (1993) 3894–3908.
[31] A.P. Siebesma, J.W.M. Cujipers, Evaluation of parametric assumptions for shallow cumulus convection, J. Atmos. Sci. 52 (6) (1995) 650–666.
[32] A.P. Siebesma, C.S. Bretherton, A. Brown, A. Chlond, J. Cuxart, P.G. Duynkerke, H. Jiang, M. Khairoutdinov, D. Lewellen, C.-H. Moeng, E. Sanchez, B. Stevens, D.E. Stevens, A large eddy simulation inter-comparison study of shallow cumulus convection, J. Atmos. Sci. 60 (10) (2003) 1201–1219.
[33] A. Dipankar, P. Sagaut, Characteristics of electromagnetic wave propagation in moist convective boundary layer using large eddy simulation, (2009), submitted for publication.
[34] A. Tunick, CN2 model to calculate the micrometeorological influences on the refractive index structure parameter, Environ. Model. Soft. 18 (2003) 165–171.
[35] R.J. Hill, Models of the scalar spectrum for turbulent advection, J. Fluid Mech. 88 (1978) 541–562.
[36] S.B. Pope, Turbulent Flows, Cambridge University Press, 2000.